Neutron Imaging with Bragg Mirrors

Alexandru Dan Stoica[*a], Xun Li Wang[a], Mihai Popovici[b] and Camden Hubbard[c]

[a]Spallation Neutron Source (SNS), Oak Ridge National Laboratory (ORNL), Oak Ridge, TN
[b]University of Missouri Research Reactor (MURR), Columbia, MO
[c]Metals and Ceramic Division, Oak Ridge National Laboratory (ORNL), Oak Ridge, TN

ABSTRACT

Phase-space analysis of neutron optics has revealed that neutron imaging by Bragg reflection from thick bent perfect crystals can be non-dispersive (independent of the neutron wavelength), like with an optical mirror. The corresponding devices, called Bragg mirrors (BM), can be used for neutron imaging at pulsed neutron sources. Using a position sensitive detector (PSD) and time-of-flight analysis (TOF), a BM imaging system will make it possible to collect both real space mapping data and scattering space data simultaneously. Each pixel of PSD will correspond to a point in the sample and will contain a segment of the diffraction pattern (useful for strain, texture or phase analysis), or of an inelastic spectrum. In this paper the resolution and efficiency of BM in TOF diffraction experiments are calculated and compared with the usual sequential method of mapping. Experimental tests performed at steady state neutron sources showed sub-millimeter spatial resolution in the one-dimensional case.

Keywords: neutron imaging, time-of-flight diffraction, Bragg optics, pulsed neutron source

1. INTRODUCTION

Attempts to use bent perfect crystals as neutron monochromators originate in early seventies[1]. Understanding the focusing resources of bent crystals and the increase of reflectivity of perfect crystals by straining[2,3] has led to progress of these ideas. Thanks to the high transparency of silicon to thermal neutrons, thick monochromator crystals can be used. However, focusing applications often demand strong curvatures that cannot be reached because of the breakage. A solution is to build effectively thick crystals from packets of thin wafers. This idea was first experimented long ago[4-7], but was not implemented in neutron monochromator construction until recently.[8]

Theoretical examination of neutron imaging by Bragg reflection from bent crystals was undertaken recently.[9,10] A result that came as a surprise was that thick multi-wafer packets can provide sharp imaging even if the incident beam has a broad distribution of wavelengths. The image blurring is canceled when two conditions of non-dispersive imaging are met (non-dispersive = independent of wavelength). With thick packets of silicon wafers the spatial resolution of the non-dispersive image is limited by the thickness of a single wafer rather than by the overall thickness of the packet. Such devices have been called Bragg mirrors (BM).

In time-of flight (TOF) diffraction, a BM together with one-dimensional (1D) or two-dimensional (2D) position sensitive detection (PSD) allows simultaneous mapping in both real space and scattering space. The use of BM is being considered for VULCAN, the dedicated engineering diffractometer at the Spallation Neutron Source under construction in the US, with the aim of achieving 0.1 mm spatial resolution of mapping the sample.

2. MATRIX DESCRIPTION OF DIFFRACTION BY STRAINED PERFECT CRYSTALS

Neutron diffraction by strained perfect crystals can be described in the quasi-classical limit[11] in terms of geometrical optics (particle approach). The local value of the reciprocal lattice vector is defined for every point of the crystal[3]. Neutrons along a given path in the crystal are reflected with a certain probability at the points where the Bragg condition is fulfilled.[12] This is

[*] stoicaad@ornl.gov; phone 1 865 574-0350; fax 1 865 241-5177; Spallation Neutron Source, 701 Scarboro Road, Oak Ridge, TN, USA 37830

an extension of the simple lamellar model of diffraction that was proposed earlier[1]. The approach neglects the spatial extent of dynamic diffraction (~ 10^{-3} mm) and the angular dynamic range (~ 10^{-6} rad.).

A matrix method using the corpuscular approach similar to that of Gaussian lens optics was worked out for neutron optics.[2,13] The neutron state is specified by the spatial coordinates across the beam (y_0,z_0), the angular deviations (γ_0,δ_0) from the beam axis and the relative deviation of the wavevector ($\Delta k_0/k$). Linear relations between consecutive neutron states along the path describe the variation of these parameters. To simplify the calculations the neutron state is specified only in a few locations.

In the paraxial approximation of linear relations describing the Bragg reflection, the neutron coordinates in the horizontal (diffraction) plane are decoupled from those in the vertical (sagittal) plane and the wavevector deviation has no influence on the vertical motion. One can thus consider separately the vectors $\eta_0 =(y_0, \gamma_0, \Delta k_0/k)$ and $\eta_1 =(y_1, \gamma_1, \Delta k_1/k)$ of the neutron state in the horizontal plane and the vectors $\zeta_0 = (z_0,\delta_0)$ and $\zeta_1 = (z_1,\delta_1)$ in the vertical plane. The concept of acceptance diagrams [14] is quite useful to visualize the allowed domains of these vectors - the phase space acceptance windows.

Let us first consider the simplest case of a thin curved crystal. Then a lens description of Bragg reflection can be used[13]:

$$\begin{bmatrix} y_1 \\ \gamma_1 \end{bmatrix} = \begin{bmatrix} \dfrac{L_1 - f_1}{f_0} & \dfrac{L_0 L_1}{f_0}\left(1 - \dfrac{f_0}{L_0} - \dfrac{f_1}{L_1}\right) \\ \dfrac{1}{f_0} & \dfrac{L_0}{f_0} - 1 \end{bmatrix} \times \begin{bmatrix} y_0 \\ \gamma_0 \end{bmatrix}, \tag{1}$$

with L_0 the distance to the crystal from the point where the initial state is considered, L_1 the distance from the crystal to the point where the final state is considered, and f_0 and f_1 the focal lengths before and after Bragg reflection:

$$f_0 = \frac{R_e}{2}\sin(\theta + \chi)\,\mathrm{sgn}(\theta + \chi)\,;\, f_1 = \frac{R_e}{2}\sin(\theta - \chi)\,\mathrm{sgn}(\theta + \chi)\ , \tag{2}$$

where R_e is the radius of curvature of the crystal in the horizontal (equatorial) plane, θ and χ are the crystal Bragg and cutting angles, respectively (see Fig. 1). R_e is defined as positive if neutrons strike the concave side of the crystal. By equating to zero the upper right element of the coupling matrix one gets the well-known focusing relation for lenses:

$$\frac{f_0}{L_0} + \frac{f_1}{L_1} = 1\ . \tag{3}$$

When relation (3) is satisfied all neutrons emerging from a point arrive to another point regardless of direction: a point is imaged by reflection into a point. The ratio $M=y_1/y_0$ – the magnification - becomes then $M=L_1/L_0$. This is also valid for the image magnification in the vertical plane. The matrix description of the image formation in the vertical plane is similar and within the paraxial lens optics the results are formally the same.

In the diffraction plane the wavevector is correlated with the direction through the Bragg law. For bent perfect crystals of negligible thickness one has[13]:

$$\begin{aligned} \frac{\Delta k_0}{k} &= -\cot\theta\,\frac{y_0}{2f_0} - \cot\theta\left(\frac{L_0}{2f_0} - 1\right)\gamma_0 \\ \frac{\Delta k_1}{k} &= -\cot\theta\,\frac{y_1}{2f_1} + \cot\theta\left(\frac{L_1}{2f_1} - 1\right)\gamma_1 \end{aligned} \tag{4}$$

The wavevector deviations before and after diffraction are in fact equal, but separate notations are kept to allow for the Doppler effect and other possible inelastic phenomena.

The effect of the crystal thickness leads to a blurring of the ideal picture described by relations (1) and (4). Wavevectors are no longer restricted to the values prescribed by (4) and the neutron trajectory is not exactly determined by (1). Relations (4) still define the inclination of the acceptance window in the ($k\gamma$ Δk) plane of the phase space. To describe analytically the blurring due to the crystal thickness the evolution along the neutron beam of the full three-dimensional vector η is considered. A 3x3 reflection matrix relating the horizontal vectors η_1 and η_0 describes the change of neutron state on diffraction as the diffraction by perfect crystals is basically a deterministic process. The coordinates of the point in the crystal

where diffraction takes place are eliminated in the process but are accounted for in the boundaries of the phase space acceptance window.

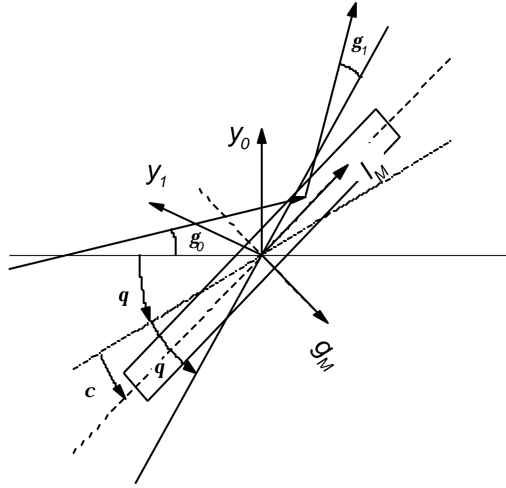

Fig. 1: Geometry of the diffraction process in real space.

Within the first order (linear, or paraxial) approximation, the relations describing the local diffraction conditions inside a strained (possibly moving) crystal are obtained by expanding the Bragg relation in vector form. To calculate the neutron trajectories before and after reflection one needs to know the spatial variation of the components of the reciprocal-lattice vector along the reciprocal-lattice vector of the unbent crystal, $\boldsymbol{t_0}$, and perpendicular to it in the diffraction plane, and the local lattice velocity component along $\boldsymbol{t_0}$. In the first order the relation defining the reflection matrix is:

$$\begin{bmatrix} y_1 \\ \boldsymbol{g}_1 \\ \frac{\Delta k_1}{k} \end{bmatrix} = \begin{bmatrix} C_{11} & C_{12} & C_{13} \\ C_{21} & C_{22} & C_{23} \\ C_{31} & C_{32} & C_{33} \end{bmatrix} \times \begin{bmatrix} y_0 \\ \boldsymbol{g}_0 \\ \frac{\Delta k_0}{k} \end{bmatrix} \tag{5}$$

A constraint matrix defining the phase space acceptance diagram is defined similarly. It relates the true crystal coordinates l_M and g_M (see Fig.1) with the variables of the neutron path before reflection y_0, $\boldsymbol{g}_0$, $\boldsymbol{D}k_0/k$ (or after reflection):

$$\begin{bmatrix} l_M \\ g_M \end{bmatrix} = \begin{bmatrix} A_{11} & A_{12} & A_{13} \\ A_{21} & A_{22} & A_{23} \end{bmatrix} \times \begin{bmatrix} y_0 \\ \boldsymbol{g}_0 \\ \frac{\Delta k_0}{k} \end{bmatrix} \tag{6}$$

To describe packets of wafers a simple model is used: that of a bulk bent crystal of a thickness corresponding to the total thickness of the packet but with no elastic stresses (*ideal bending*). The results are only approximate, the degree of approximation being given by the thickness of a single wafer. In fact, each bent wafer of a packet reflects neutrons like a bulk crystal and has its individual acceptance window in the phase space. The overall acceptance window has a complex shape and generally is sparsely filled. The effective peak reflectivity is an average over the whole acceptance window. When individual acceptance windows superpose, corrections must be introduced in the peak reflectivity to account for possible losses due to multiple reflections[15].

The reflection matrix for a bent packet of wafers of uniform curvature is [15]:

$$\begin{bmatrix} y_1 \\ \boldsymbol{g}_1 \\ \frac{\Delta k_1}{k} \end{bmatrix} = \begin{bmatrix} \frac{L_1^*}{L_0^*} & -2L_1^* & 2L_1^* \tan \boldsymbol{q} \\ 0 & 1 & -2\tan \boldsymbol{q} \\ 0 & 0 & 1 \end{bmatrix} \times \begin{bmatrix} y_0 \\ \boldsymbol{g}_0 \\ \frac{\Delta k_0}{k} \end{bmatrix}, \tag{7}$$

where

$$L_0^* = \frac{R_e \sin 2\boldsymbol{q} \, \mathrm{sgn}(\boldsymbol{q} + \boldsymbol{c})}{2\cos(\boldsymbol{q} - \boldsymbol{c})}; \; L_1^* = \frac{R_e \sin 2\boldsymbol{q} \, \mathrm{sgn}(\boldsymbol{q} + \boldsymbol{c})}{2\cos(\boldsymbol{q} + \boldsymbol{c})} \, . \tag{8}$$

The determinant of the reflection matrix is $cos(\boldsymbol{q}-\boldsymbol{c})/cos(\boldsymbol{q}+\boldsymbol{c})$. It differs from unity if the reflection is asymmetric. The overall volume in the phase space diagram may thus be different before and after reflection. This is an apparent violation of the Liouville theorem, introduced by the approximation used in modeling. In reality no violation occurs, as each individual wafer does obey the Liouville theorem. To correct for this, a factor must be introduced in the average peak reflectivity, which comes to depend on whether the phase space volume considered on averaging is before or after reflection.[15] This only matters for intensity calculations. We will focus here on optical properties and will assume that the conservation of phase space density is ensured through peak reflectivities.

In the multi-wafer case relations (6) leads to the following restrictions[15]:

$$\begin{bmatrix} -\frac{g_M^{\max}}{2} \\ -\frac{l_M^{\max}}{2} \end{bmatrix} \le \begin{bmatrix} -\frac{1}{\cos(\boldsymbol{q} + \boldsymbol{c})} & \frac{2f_0}{\cos(\boldsymbol{q} + \boldsymbol{c})} & -\frac{2f_0}{\cos(\boldsymbol{q} + \boldsymbol{c})} \tan \boldsymbol{q} \\ 0 & \frac{2f_0}{\sin(\boldsymbol{q} + \boldsymbol{c})} & -\frac{2f_0}{\sin(\boldsymbol{q} + \boldsymbol{c})} \tan \boldsymbol{q} \end{bmatrix} \times \begin{bmatrix} y_0 \\ \boldsymbol{g}_0 \\ \frac{\Delta k_0}{k} \end{bmatrix} \le \begin{bmatrix} \frac{g_M^{\max}}{2} \\ \frac{l_M^{\max}}{2} \end{bmatrix} \tag{9}$$

where g_M^{max} and l_M^{max} are the total thickness and lateral extent of the packet. The wafer packet was considered parallel, with the wafers fully in contact on adjacent surfaces. If adjacent wafers are not in contact and relative tilts are introduced, then formulae (7) and (8) will change.

3. IMAGING CONDITIONS

Consider the transfer of a neutron from a point at a distance L_0 before the crystal to a point at a distance L_1 after the crystal. Taking into account the matrix of transport in free space, the general expression relating the final state with the initial state can be rearranged as follows:

$$\begin{bmatrix} y_1 \\ \boldsymbol{g}_1 \\ \frac{\Delta k_1}{k} \end{bmatrix} = \begin{bmatrix} C_{11} + L_1 C_{21} & C_{12} + L_0 C_{11} + L_1 C_{22} + L_0 L_1 C_{21} & C_{13} + L_1 C_{23} \\ C_{21} & C_{22} & C_{23} \\ C_{31} & C_{32} & C_{33} \end{bmatrix} \times \begin{bmatrix} y_0 \\ \boldsymbol{g}_0 \\ \frac{\Delta k_0}{k} \end{bmatrix} \tag{10}$$

The structure of this matrix gives an interesting result: neutrons emerging from a point at L_0 are imaged into a point at L_1 when the following correlation between $\boldsymbol{g}_0$ and $\boldsymbol{D}k_0/k$ exists:

$$\left(C_{12} + L_0 C_{11} + L_1 C_{22} + L_0 L_1 C_{21}\right)\boldsymbol{g}_0 + \left(C_{13} + L_1 C_{23}\right)\frac{\Delta k_0}{k} = 0 \tag{11}$$

In the general case relation (11) says that a point of the object space may be imaged into different points of a line. Every point of the line in the diffraction plane will correspond to a distinct path in the wavevector plane ($k\boldsymbol{g}_0$, $\boldsymbol{D}k_0$). The linear image will supply a spectral analysis of the object. This is analogous to what a prism does in conventional optics. Only a small part of the crystal will contribute to the formation of each image point. Different zones of the crystal will give different points of the image. In a terminology borrowed from conventional optics this is the case of *dispersive imaging*.[9,10] The object point is

imaged into a line along which some physical quantity varies (wavevector, wavevector transfer, energy transfer, etc). The distribution of that physical quantity is converted into a spatial distribution.

If the task is to get a real image of the object, then the image of a point should not be a line but a point. The arrangement must be non-dispersive, that is the spatial dispersion of the beam must be canceled. The contributions to the blurring from both the angular spread and the wavevector spread must vanish. Then the crystal becomes a *Bragg mirror* (BM) - an imaging device with no chromatic aberrations. For the crystal to be a Bragg mirror the coefficients of both the γ_0 and $\Delta k_0/k$ terms of y_1 in relation (11) must vanish simultaneously:

$$\begin{aligned} &C_{12} + L_0 C_{11} + L_1 C_{22} + L_0 L_1 C_{21} = 0, \\ &C_{13} + L_1 C_{23} = 0 \end{aligned} \qquad (12)$$

or, equivalently:

$$L_0 = -\frac{\begin{vmatrix} C_{12} & C_{13} \\ C_{22} & C_{23} \end{vmatrix}}{\begin{vmatrix} C_{11} & C_{13} \\ C_{21} & C_{23} \end{vmatrix}}; L_1 = -\frac{C_{13}}{C_{23}}. \qquad (13)$$

For a curved multi-wafer packet the two conditions of non-dispersive imaging have the following form:

$$L_0 = L_0^*, L_1 = L_1^*, \qquad (14)$$

with L_0^* and L_1^* defined by the relations (8).

For multi-wafer packets the magnification of the BM given by the distance ratio becomes:

$$M = \frac{\cos(\theta - \chi)}{\cos(\theta + \chi)} \qquad (15)$$

A curved multi-wafer will deliver an image whenever the relation (3) is fulfilled, but the image will be non-dispersive only for a magnification prescribed by (15). Only when $M > 0$ is the image real and only then can a BM provide an image on a PSD. The BM working zones for ideal bending are sketched in Fig. 2 as a function of the take-off angle 2θ and $\alpha=\theta+\chi$ (BM inclination angle relative to the incoming beam). Reflection arrangements are permitted at any take-off angle.

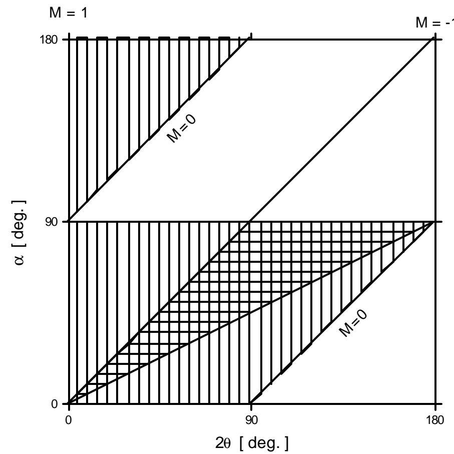

Fig. 2: Bragg Mirror working zones as a function of the take-off angle 2θ and the inclination angle relative to the incoming beam $\alpha=\theta+\chi$; vertical grating – real image; cross hatched zone – real image, reflection geometry, M>1.

A mirror is *astigmatic* if the image positions in the equatorial and sagittal planes are different. The astigmatism of the BM is canceled *(stigmatic imaging)* when the lens focusing relation in the vertical plane is also fulfilled. This leads to a connection between the sagittal (vertical) curvature radius R_a and the equatorial (horizontal) curvature radius R_e. A simple relation follows for multi-wafer packets with ideal bending:

$$R_a = R_e \operatorname{sgn}(\theta + \chi) \sin^2 \theta \qquad (16)$$

The spatial resolution of the image is determined by the optical quality of the BM and by the spatial resolution of the PSD, as the image blurring due to the intrinsic diffraction range in a perfect crystal is usually negligible (less that 5 μm at one meter of distance). For curved multi-wafer packets the main aberration term comes from the elastic deformation of the wafers. A tangential stress gradient is generated inside the crystal on curving. This gradient not only changes the d-spacing, but also rotates the crystalline planes if they are not parallel to the crystal surface. The aberration term due to wafer deformation is proportional to $\sin\chi$ and to the wafer thickness. Consequently this term vanishes when $\chi=0$. Otherwise it can be minimized with thinner wafers that are available commercially down to 10 microns. The mechanics of assembling very thin wafers would complicate, though. Possible imperfections of the device (wafer misalignment, non-uniformity of the thickness and of the horizontal radius) will give rise to additional blurring. The practical limit of spatial resolution is expected to be around 100 microns. A very high accuracy of bending will be needed for reaching that limit.

4. BRAGG MIRROR AT PULSED SOURCE

A BM can also be used for neutron imaging at pulsed neutron sources. Then the incident neutron energy is determined by time-of-flight (TOF). By using a 2-D PSD and TOF analysis, the BM imaging system (BMIS) will make it possible to collect real space mapping data and scattering space data simultaneously, enabling totally new research opportunities. To study the image formation in that case it is necessary to add the TOF coordinate to the matrix formalism introduced before. The relation (7) corresponding to curved packets of wafers changes in a four dimensional formulation as follow:

$$\begin{bmatrix} y_1 \\ \gamma_1 \\ \dfrac{\Delta k_1}{k} \\ \Delta t_1 \end{bmatrix} = \begin{bmatrix} M & -2L_1^* & 2L_1^* & 0 \\ 0 & 1 & -2\tan\theta & 0 \\ 0 & 0 & 1 & 0 \\ -\dfrac{2\sin\theta\cos\chi}{v_n\cos(\theta+\chi)} & \dfrac{2L_1^*\tan\theta}{v_n} & -\dfrac{2L_1^*\tan^2\theta}{v_n} & 1 \end{bmatrix} \times \begin{bmatrix} y_0 \\ \gamma_0 \\ \dfrac{\Delta k_0}{k} \\ \Delta t_0 \end{bmatrix} \tag{17}$$

where Δt is the time deviation from the nominal value, v_n is the average neutron velocity and M is the BM magnification as defined by (15). In this simple case the imaging conditions (12) – (14) are still valid. The image position does not depend of time, but this formalism allows calculating the TOF spread by introducing the flight history through a general matrix of transport in free space along a flight path L:

$$\begin{bmatrix} y_1 \\ \gamma_1 \\ \dfrac{\Delta k_1}{k} \\ \Delta t_1 \end{bmatrix} = \begin{bmatrix} 1 & L & 0 & 0 \\ 0 & 1 & 0 & 0 \\ 0 & 0 & 1 & 0 \\ 0 & 0 & -\dfrac{L}{v_n} & 1 \end{bmatrix} \times \begin{bmatrix} y_0 \\ \gamma_0 \\ \dfrac{\Delta k_0}{k} \\ \Delta t_0 \end{bmatrix} \tag{18}$$

Considering the elastic (or quasi-elastic) scattering, the contributions of the horizontal angular deviation after scattering γ_0, and of the relative wavevector deviation $\Delta k/k$, to the final TOF relative deviation $\Delta t_f/t_f$ are given by:

$$\frac{\Delta t_f}{t_f} = (M-1)\frac{L_{SM}}{L_T}\tan\theta\,\gamma_0 + \left(1 + 2M\frac{L_{SM}}{L_T}\tan^2\theta\right)\frac{\Delta k}{k} \tag{19}$$

where L_{SM} is the distance from sample to BM and L_T is the total flight path length from neutron source to detector. Using relation (19) one can evaluate the TOF resolution for different experimental imaging problems. The image may refer to any scattering law, for either elastic or inelastic scattering.

One possibility is to use BM as an analyzer to define the scattered neutron energy. The most favorable configuration in this case is the symmetric reflection BM with $M = 1$. Then the angular deviation contribution to TOF resolution is canceled. The contribution of BM to the TOF resolution is determined by the BM thickness, g_M^{max}, as follows:

$$\left(\frac{\Delta t_f}{t_f}\right)_{BM} = \left(\cot\theta + 2\frac{L_{SM}}{L_T}\tan\theta\right)\cos\theta\,\frac{g_M^{max}}{L_{SM}} \tag{20}$$

The TOF resolution and the BM angular acceptance are presented in Fig. 3 for a standard BM configuration with a 1% ratio of the BM thickness to L_{MS}, and a BM aspect ratio of 10 (ratio of lateral extent to thickness).

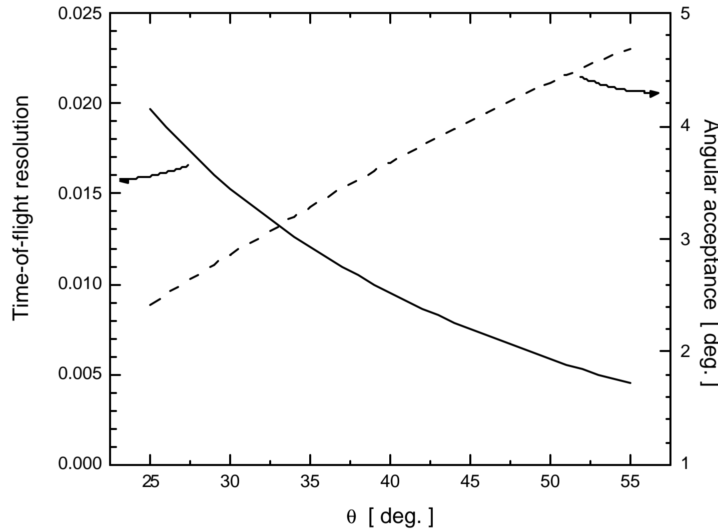

Fig. 3: Bragg mirror time of flight resolution and angular acceptance for quasi-elastic scattering.

Another possibility is to use BM for imaging in diffraction. In this case each pixel of PSD contains a segment of the diffraction pattern, useful for strain, texture or phase fraction mapping. The symmetric reflection BM is not a good solution for imaging in diffraction when magnifying configurations ($M>1$) are of main interest. Because in powder diffraction the measured quantity is the reciprocal lattice vector $\boldsymbol{t}$, it is appropriate to examine the relative resolution and the acceptance window defined with respect to the reciprocal lattice vector coordinate (or equivalently the lattice spacing coordinate). The analytical results are too complex to be shown here. Numerical evaluations presented in Fig. 4a and b will only be discussed.

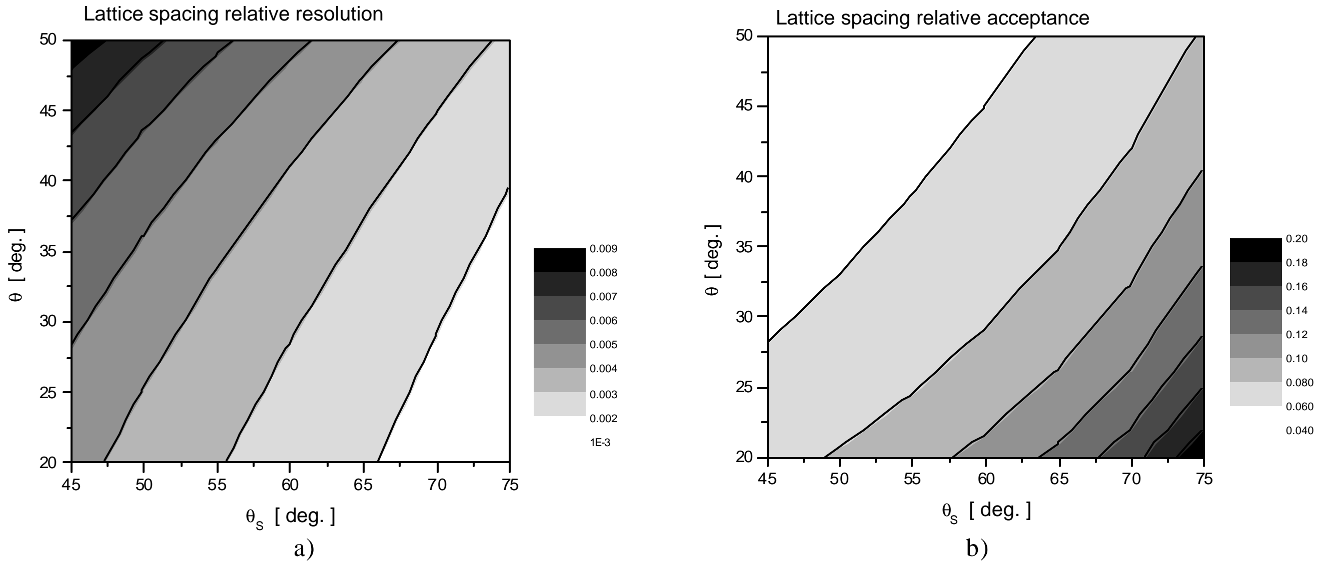

Fig. 4: Bragg mirror in time of flight diffraction: a) resolution and b) angular acceptance as functions of scattering angle $\boldsymbol{q}_S$ (detector angle is $2\boldsymbol{q}_S$) and device Bragg angle, $\boldsymbol{q}$.

The results shown in Fig. 4a include the contribution of the incoming beam angular divergence. This contribution was taken equal to the BM contribution to reach the maximum intensity. The corresponding divergences of the incoming beam are set in the range of 6 – 12 mrad, depending on the BM configuration. The same standard BM configuration with a 1% ratio of the BM thickness to L_{MS} and an aspect ratio of 10 was considered. It can be seen that at $2\boldsymbol{q}_S = 90^0$ (the most attractive case for imaging in scattering) lattice spacing resolutions better then 0.5% can be achieved with a relative acceptance window wider than 6%. The performance is gradually improving at higher scattering angles. It is possible to record a single diffraction line or a few close lines along with their higher orders.

To broaden the lattice spacing acceptance window the BM can be rotated synchronously with the neutron burst. The acceptance window in the $(\gamma\ \Delta k/k)$ plane will then move following the variation of Bragg angle on rotation. In this way a BM can be made to reflect a large TOF spectrum of neutrons. The proposed four-dimensional matrix formalism is capable to account for this complex situation. Unfortunately all matrix elements in (17) became different from zero and the analytical expressions are too intricate for this discussion. The image is moving across PSD and it is necessary to consider a mixture of focusing in space and in time. A good understanding of the BM rotation is not available at this time.

5. TESTING THE BRAGG MIRROR CONCEPT

Experimental tests were made at the University of Missouri Research Reactor (MURR) to prove some basic features of BM arrangements. The experiments on non-dispersive imaging were done with the standard PG monochromator of the TRIAX instrument, horizontally flat and vertically focusing. The mosaic spread of PG led to a large angular and spatial spread of the beam and to a sufficiently broad wavelength band. The object was a cadmium plate with three slits 0.5 mm wide and 3 mm apart. The image was brought to the computed position by varying the analyzer curvature. It was registered on Polaroid film and scanned with a narrow (0.2 mm) slit. To simulate the white beam associated with a TOF arrangement the incident neutron wavelength was varied. Because of the limited beam angular divergence (less than 1 degree), a full mapping of the phase space acceptance window could not be achieved, though.

Measurements with a single wafer were done first to show the ultimate resolution in imaging achievable with a BM. A magnifying configuration was chosen to minimize the wafer thickness (0.7 mm) contribution and the PSD smearing in a real design. The image obtained with the (220) reflection from a Si [111] wafer at a magnification of 2.8 is shown in fig. 5a. A 2D position-wavelength scan of this image is shown in fig. 5b. To facilitate the comparison of different BM configurations, in fig. 5b the detector angular position was converted into the coordinate across the object and the monochromator angle was converted into the relative variation of wavelength. The FWHM corresponding to a single slit on the coordinate scale at object is of only 0.54 mm, proving very little smearing. The position of the image is seen to not depend indeed on the wavelength. This is quite remarkable, as with Bragg reflection one would expect everything to depend on the Bragg angle.

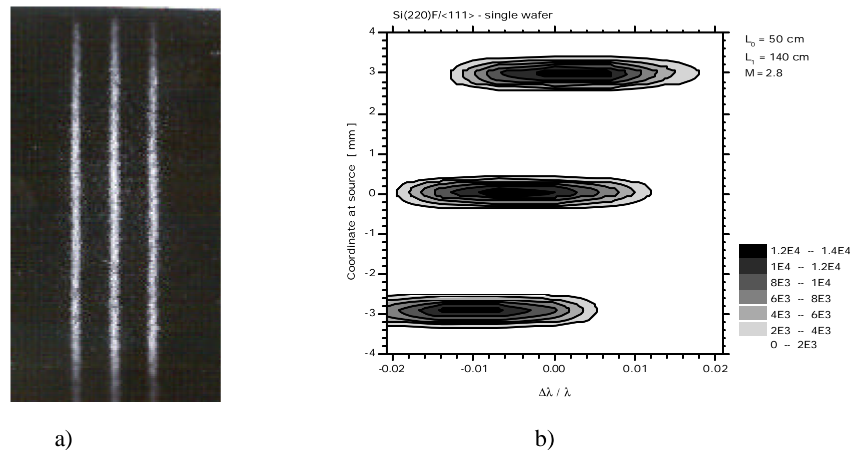

a) b)

Fig. 5: Neutron imaging with one wafer (2.8 magnification): a) – photo; b) – 2D scan as function of incident neutron wavelength.

By considering the standard deviation of the peak profile and subtracting the contributions of the object slit and the receiving slit, one gets a spatial resolution delivered by one wafer in BM configuration of less than 0.28 mm FWHM in the Gaussian approximation. Spatial resolutions down to 0.1 mm should be obtainable by reducing the wafer thickness by a factor of 2-3.

A good quality of wafer surface is required for such a resolution. Test measurements using an as-cut wafer showed a dramatic smearing of the image. A scan of the image obtained with a single unpolished wafer in symmetric (220) reflection is shown in fig. 6a. The pattern should be compared with the image scan presented in fig. 6b, corresponding to a packet of 13 mirror-polished wafers of the same orientation. The peaks are almost twice broader with the as-cut wafer. This is the effect of the strain in the superficial layers induced by surface roughness.

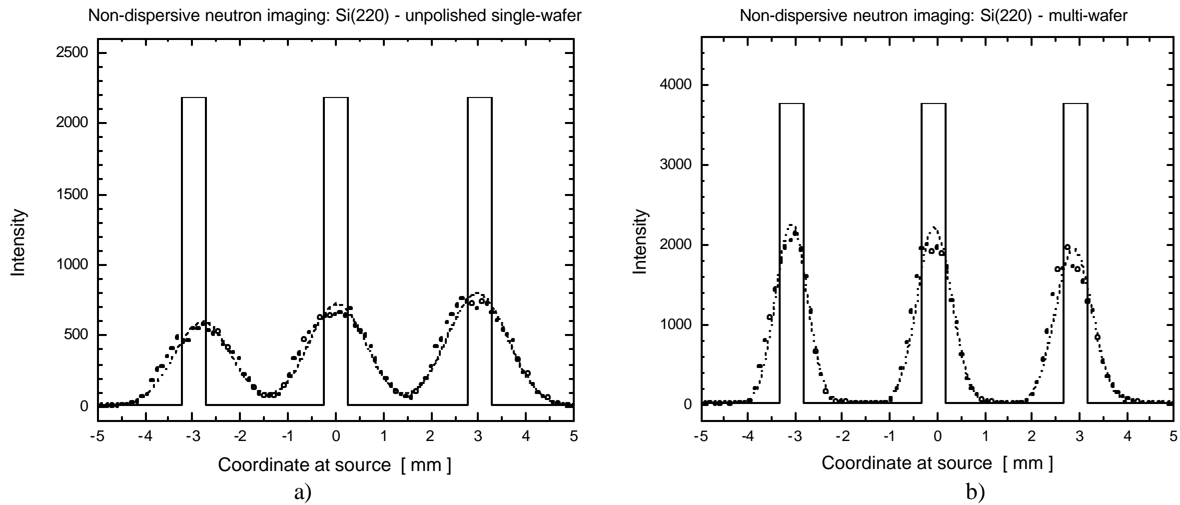

a) b)

Fig. 6: Neutron imaging in symmetric reflection (unit magnification): a) – single unpolished wafer; b) – multi-wafer.

Three multi-wafer silicon units constructed at MURR have been tested to investigate the imaging capability in different BM configurations. The maximally achieved magnification was smaller than that obtained for single wafers due to the limitation of the device curvature. The results obtained with the (311) reflection from a Si multi-[100]-wafer are presented in fig. 7.

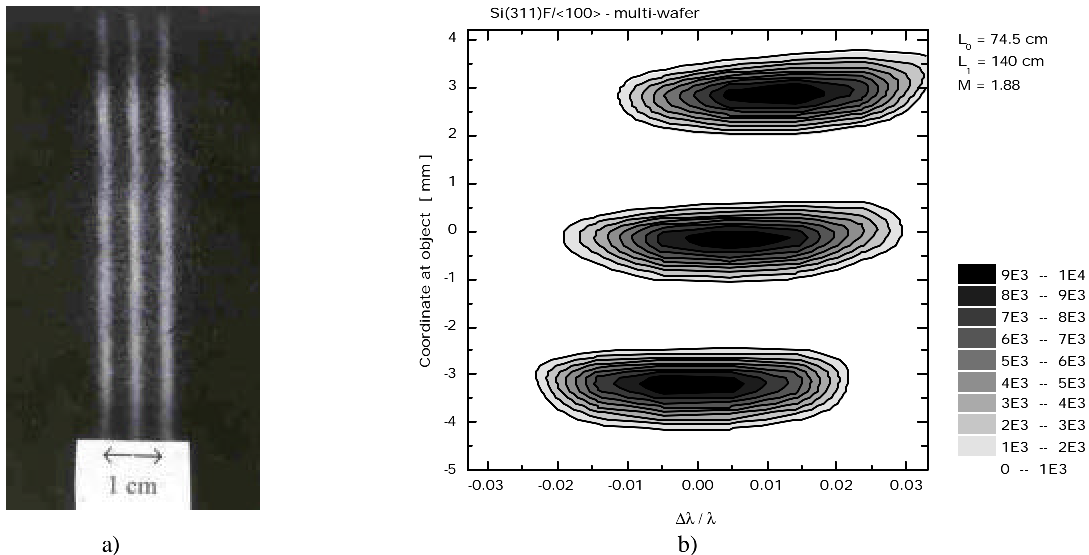

a) b)

Fig. 7: Neutron imaging with multi-wafers (1.88 magnification): a) – photo; b) – 2D scan as function of incident neutron wavelength.

The assembly consisted of 14 commercial wafers, each 18 cm wide and 0.7 mm thick, originating from the same [100] ingot. The horizontal radius of curvature R_e was set by a 4-point elastic bending device and was adjustable with a fine screw. The vertical curvature was approximated by fine segmentation (5 mm). The vertical radius R_a was set by the profile of the bending posts (barrel shaped on the front, concave on the back) and was fixed at 1.38 m. Because the vertical radius was fixed and the vertical curvature was obtained by segmentation, the astigmatism was not canceled in this experiment. The (311) asymmetric reflection gave a magnification of 1.88 in beam condensation (Fankuchen) setting. The image is seen to be sharp in spite of the 10.3 mm packet thickness and the broad wavelength band of the neutron beam. Additional image smearing comes from inter-wafer disorientation and misalignments. The non-uniform intensity distribution across the height indicates that the misalignments are not so much due to wafers in a given bundle but rather to different bundles. The influence of all uncontrolled smearing influences can be evaluated by defining an overall slope error, which is an equivalent lattice rotation producing the same smearing effect.

Table 1

Wafer orientation	Diffraction line	λ [Å]	θ [deg]	χ [deg]	M	FWHM exp [mm]	St. dev. theoretic [mm]	FWHM residual [mm]	Slope error [mrad]
1	*2*	*3*	*4*	*5*	*6*	*7*	*8*	*9*	*10*
<111> s	(220)	2.36	37.8	31.3	2.80	0.54	0.168	<0.27	<0.27
<100> m	(311)	1.78	32.9	25.2	1.88	0.69	0.194	0.51	0.35
<511> m	(422)	1.15	31.2	19.5	1.55	1.01	0.210	0.88	0.48
<511> m	(400)	1.48	33.0	15.8	1.45	1.00	0.214	0.87	0.45
<110> m	(331)	1.40	34.2	13.3	1.38	0.99	0.160	0.92	0.46
<110> m	(220)	2.36	37.8	0	1.00	0.85	0.155	0.76	0.31
<110> s	(220)	2.36	37.8	0	1.00	1.44	0.155	1.40	0.57
<100> m	(331)	1.59	29.0	-25.2	0.59	1.44	0.491	1.38	0.57

Table 1 summarizes the test results obtained with different devices and configurations. Column 1 specifies the reflection with *s* for single wafer and *m* for multi-wafer. Experimental FWHM values of the image of one slit are given in column 7. The standard deviations of the theoretical profile including the contributions of slits and the thickness contribution of the elastically deformed single wafer are shown in column 8. The real FWHM after extracting the contribution of the object slit are given in column 9, and the resulting slope errors computed as FWHM of a Gaussian distribution in column 10. The slope error varies from 0.3 to 0.5 mrad in symmetric and beam condensation configurations depending of the device quality. For comparison the results for polished and unpolished single wafers are also presented in lines 1 and 7. According to these data the slope error corresponding to the existing devices cannot provide a spatial resolution better than 0.5 mm, and the slope error introduced by surface roughness is larger than the multi-wafer imperfection.

Another test measurement was completed at the High Flux Isotope Reactor (HFIR) of the Oak Ridge National Laboratory (ORNL) at the residual stress machine. The thick multi-wafer assembly was placed in the neutron beam scattered by the sample. A PSD was used. The PSD contribution had a Gaussian profile with 2.7 mm FWHM. An additional increase of the FWHM up to 3.2 mm was observed at the larger angular divergence of the incoming neutron beam.

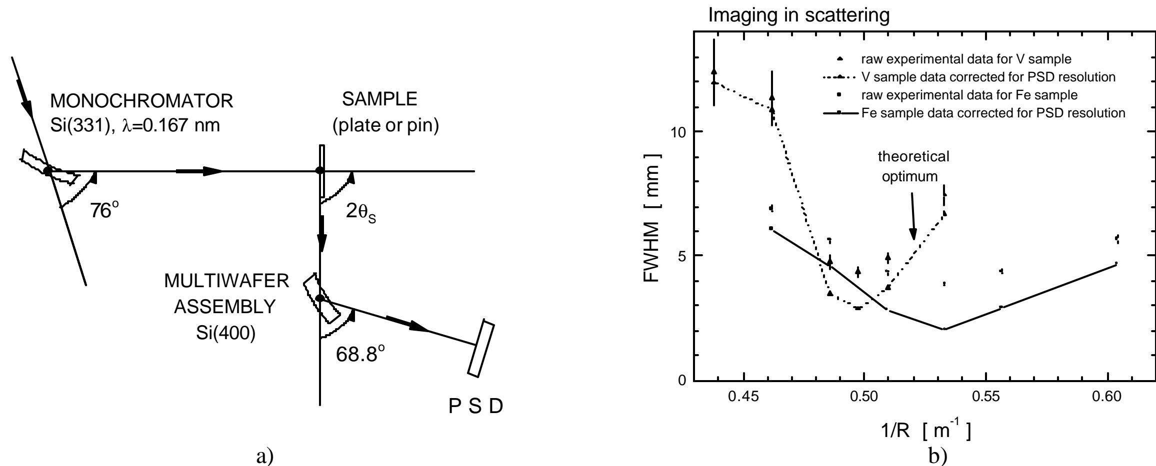

Fig. 8: Neutron imaging in scattering: a) – BM experimental set-up; b) – imaging test data for incoherent scattering and diffraction.

The current silicon monochromator of the ORNL residual stress machine provided a monochromatic beam with λ=1.67 **Å**. Two different samples were tested for imaging in scattering: a vanadium plate 2 mm thick and an iron pin (diameter of ~2 mm). The multi-wafer assembly with the Si (400) reflection intercepted the scattered neutron beam and provided the image of the sample on the PSD (fig. 8a). For the iron pin sample the multi-wafer assembly was placed at 81.9° take-off angle corresponding to the (211) diffraction line. For the vanadium plate the neutron scattering is elastic, incoherent and isotropic, consequently the scattering angle was chosen for alignment reasons at 86.9°. The plate was oriented along the scattered beam

to minimize the spatial extension of the scattered neutron beam at the sample position. The distances from sample to multi-wafer and from multi-wafer to PSD were almost equal (1.09 m).

The curvature of the multi-wafer assembly was varied to get the sharpest image. The FWHM of the spatial pattern recorded by PSD is presented in fig. 8b. The optimal curvatures are slightly different from the theoretical value, but these differences are not significant enough. By contrast the minimal FWHM's of images (2-3 mm) are encouraging. The image is naturally wider for the vanadium plate because the whole analyzer was contributing to its formation and all geometrical contributions to the image smearing were significantly larger than in the diffraction case when the scattered beam was spatially limited.

6. ALTERNATIVE METHODS

The simplest alternative to BM mapping by imaging is the sequential method of mapping using the pinhole approach. In comparison with it, the simultaneous BM method is able to deliver a larger number of measured points. As to the rate of data accumulation, that number should be compared to the number of detectors available in the former method. To develop the analogy let us consider in the sequential method a sampling area of 10×40 mm and a distance of 300 mm from the sample to the mapping slit. For BM the peak reflectivity will be in the range 0.2 – 0.5 and the vertical resolution in the range 2 – 5 mm (due to the segmentation method used for vertical bending). At a horizontal spatial resolution of 1 mm, one BM would thus be equivalent to $10^2 - 10^3$ detectors looking at the same pixel in the sequential method. This number increases with a factor of 100 if the pixel width decreases to 0.1 mm. The throughput of BM can be further improved if the mirror astigmatism is cancelled exactly by a continuous vertical curvature of wafers (not by segmentation).

Methods of microbeam formation used in synchrotron radiation (SR) research can also be considered for imaging in neutron scattering. Some are more promising than others.

Glancing optics: Ellipsoidal and Kirkpatrik-Baez mirrors have been used in SR focusing arrangements.[16] For this type of arrangements the angular acceptance is low, being determined by the critical angle in the equatorial plane. Multilayer mirrors can increase the angular range of specular reflection. In fact such mirrors are a sort of BM with a large d-spacing and a d-spacing gradient through the thickness. Many neutron devices are being developed in this area but none has been yet designed for imaging.
Polycapillary optics has shown exciting capabilities to focus neutrons at a submillimeter scale[17]. However, the devices designed on this principle have a modest transmission (less than 10%). The reported flux gains are basically given by the high angular divergence at focus (usually > 10 degrees). the focusing distance is small (a few millimeters only).

Refractive optics: It seems sensible that refractive techniques[18] are only applicable to very cold neutrons and the influence of gravity complicates the lens design. For cold neutrons simply adding a large number of non-absorbing lenses can increase the refraction effect,[19] but the technical possibility to build optical devices of large aperture based on refraction has not yet been demonstrated.

Diffraction lenses - In SR microscopy zone plates and Bragg-Fresnel optics are widely used.[16] The use of such high precision devices is limited to high brilliance sources. They provide a sub-micron image resolution, but the lens dimensions have also to be very small (sub-millimeter). Promising demonstration of such device type in neutron scattering is a long way off.

7. CONCLUSIONS

By bending thick multi-wafer packets and using accurately adjusted distances and curvatures, it is possible to obtain sharp imaging in white neutron beams. These Bragg Mirror arrangements can provide image magnification similarly with how optical lenses provide magnification for light. Experiments demonstrate the capability of BM arrangements of imaging with neutrons at a spatial resolution of 0.3 mm and magnifications of about 3. To push the spatial resolution close to 0.1 mm further development of silicon multi-wafer devices is needed. Estimations show that significant advance is achievable with BM imaging in comparison with the sequential pinhole probing method.

The most interesting potential applications of BM refer to TOF diffraction. This is in spite of the fact that the BM acceptance in lattice spacing is severely limited. Some of the topics are:

- Real-time microstructure analysis of the deformation of materials under static or dynamic load (mapping peak positions & widths);

- Real-time study of phase transformations induced by diffusion or solid-state reactions (integrated intensity of selected diffraction lines *versus* time and position in sample);
- High-resolution internal strain mapping (peak positions & integrated intensities).

ACKNOWLEDGMENTS

Oak Ridge National Laboratory, managed by UT-Battelle, LLC, for the US Department of Energy under contract DE-AC05-00R22725, as part of the Spallation Neutron Source Project and the High Temperature Materials Laboratory User Program, supported this work.

REFERENCES

1. G. Egert, H. Dachs, *J. Appl. Cryst*. **3**, pp. 214-220, 1970.
2. M. Popovici, A. D. Stoica, I. Ionita, *J. Appl. Cryst*. **20**, pp. 90-101, 1987.
3. A. D. Stoica, M. Popovici, *J. Appl. Cryst*. **22**, pp. 448-454, 1989.
4. F. Frey, *Nucl. Instr. and Meth.* **115**, pp. 277-284, 1974; **125**, pp. 9-17, 1975.
5. J. Kalus, *J. Appl. Cryst*. **8**, pp. 361-364, 1975.
6. M. Th. Rekveldt, *Nucl. Instr. and Meth.* **215**, pp. 521-527, 1983.
7. A. S. Arrott, T. L. Templeton, *J. Appl. Cryst*. **18**, pp. 388-395, 1985.
8. A. D. Stoica, M. Popovici, W. B. Yelon, R. Berliner, *J. Appl. Cryst*. **33**, pp. 147-155, 2000.
9. A. D. Stoica, M. Popovici, C. R. Hubbard, *ORNL / TM2000 /* **207**, 2000.
10. A. D. Stoica, M. Popovici, C. R. Hubbard, *J. Appl. Cryst*. **34**, pp. 343-357, 2001.
11. P. Lukas, J. Kulda, *Phys. Stat. Sol*. **B 156**, pp. 41-48, 1989.
12. J. Kulda, *Acta Cryst*. **A 40**, pp. 120-126, 1984.
13. M. Popovici, A. D. Stoica, *J. Phys.* ***E****: Sci. Instr*. **16**, pp. 662-665, 1983.
14. J. R. D. Copley, *J. Neutron Res.* **1**, pp. 21-36, 1993.
15. A. D. Stoica, M. Popovici, C. R. Hubbard, S. Spooner, *ORNL / TM1999 /* **277**, 1999.
16. G. E. Ice, *X-Ray Spectrometry*, **26**, pp. 315-326, 1997.
17. H.H. Chen-Mayer, D.F.R. Mildner, V.A. Sharov, Q.F. Xiao, Y.T. Cheng, R.M. Lindstrom & R.L. Paul, *Rev. Sci. Instrum.* **68**, pp. 3744-3750, 1997.
18. B. Lengeler, C. Schroer, J. Tuemmler, A. A. Snigirev, I. Snigireva, M. Drakopoulos, *EUV, X-Ray, and Neutron Optics and Sources*, ed. C. A. MacDonald, K. A. Goldberg, J. R. Maldonado, H. H. Chen-Mayer & S. P. Vernon, SPIE Proc. Series, Vol. **3767**, pp. 320-327, 1999.
19. D. J. Bishop, *EUV, X-Ray, and Neutron Optics and Sources*, ed. C. A. MacDonald, K. A. Goldberg, J. R. Maldonado, H. H. Chen-Mayer & S. P. Vernon, SPIE Proc. Series, Vol. **3767**, pp. 320-327, 1999.